Spectroscopic Characterization of Mixed Fe−Ni Oxide Electrocatalysts for the Oxygen Evolution Reaction in Alkaline Electrolytes

James Landon,[‡] Ethan Demeter,[‡] Nilay İnoğlu,[‡] Chris Keturakis,[§] Israel E. Wachs,[§] Relja Vasić,[‖] Anatoly I. Frenkel,[‖] and John R. Kitchin*,[†,‡]

[†]U.S.-DOE National Energy Technology Laboratory, Pittsburgh, Pennsylvania 15236, United States

[‡]Department of Chemical Engineering, Carnegie Mellon University, Pittsburgh Pennsylvania 15213, United States

[§]Operando Molecular Spectroscopy & Catalysis Lab, Department of Chemical Engineering, Lehigh University, Bethlehem, Pennsylvania 18015, United States

[‖]Yeshiva University, 245 Lexington Avenue, New York, New York 10016, United States

S *Supporting Information*

ABSTRACT: Mixed Fe−Ni oxide electrocatalysts for the oxygen evolution reaction in alkaline electrolytes were synthesized using three different approaches: evaporation induced self-assembly, hard templating, and dip-coating. For each synthesis method, a peak in oxygen evolution activity was observed near 10 mol % Fe content, where the mixed metal oxide was substantially more active than the parent metal oxide electrocatalysts. X-ray diffraction (XRD) analysis showed the formation of a mixed $NiO/NiFe_2O_4$ phase at low Fe concentrations, and formation of Fe_2O_3 at compositions above 25

mol % Fe. Raman vibrational spectroscopy confirmed the formation of $NiFe_2O_4$, and did not detect Fe_2O_3 in the electrocatalysts containing up to 20 mol % Fe. X-ray absorption near edge structure (XANES) showed the Fe in the mixed oxides to be predominantly in the +3 oxidation state. Extended X-ray absorption fine structure (EXAFS) showed changes in the Fe coordination shells under electrochemical oxygen evolution conditions. Temperature programmed reaction spectroscopy showed the mixed oxide surfaces also have superior oxidation activity for methanol oxidation, and that the reactivity of the mixed oxide surface is substantially different than that of the parent metal oxide surfaces. Overall, the $NiFe_2O_4$ phase is implicated in having a significant role in improving the oxygen evolution activity of the mixed metal oxide systems.

KEYWORDS: oxygen evolution electrocatalysis, mixed metal oxides
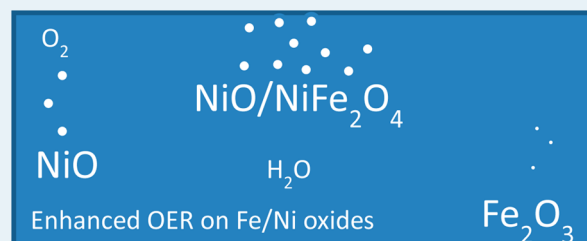
INTRODUCTION

The efficient production of hydrogen using renewable resources and energy is a key component in the development of future energy storage technologies. One method of producing hydrogen is from water electrolysis which enables H_2 production from renewable energy sources. The efficiency of this process is limited by the oxygen evolution reaction which occurs simultaneously with hydrogen evolution.

The hydrogen evolution reaction is a relatively simple reaction that readily occurs at low overpotential on many metals.[1] The oxygen evolution mechanism, in contrast, has several steps that have large reaction barriers, which lead to large required overpotentials to drive the reaction at practical rates.[2,3] The large overpotentials significantly decrease the efficiency, as the extra energy is dissipated as low quality heat, and limit the possibility of large scale production of hydrogen from water splitting. Water splitting is often performed in acidic electrolytes, where the best and most stable electrocatalysts include the oxides of Ru and Ir. A novel set of Co-based electrocatalysts that are active under neutral pH conditions

have been identified.[4−6] Still, it would be desirable to develop electrocatalysts based on considerably cheaper metals such as Ni and Fe. In acidic conditions, these metals readily corrode. Under alkaline conditions, however, some base metal oxides such as NiO become reasonably stable.[7] As these metals are significantly cheaper than the Pt-group metals, there is significant interest in understanding how to promote base metal oxide electrocatalysts for oxygen evolution

Research into oxygen evolution catalysts has been substantial and is an active research area currently.[2,8−20] Pure and mixed transition metal oxide catalysts have been examined,[9,21−27] along with investigations into structures such as perovskites,[28,29] pyrochlores, and spinels.[30,31] From this work, the best pure metal oxides for the oxygen evolution reaction include RuO_2 and IrO_2.[32,33] These metals are expensive, but

they are needed for highly acidic electrolytes because of their high stability toward corrosion.

There are reports of mixed metal oxides with oxygen evolution reactivities that are superior to that of either of the parent metal oxides. Mixed Ni−Fe oxide catalysts have been shown to be of particular interest because of the lower overpotential of reaction and the stable activity. Corrigan et al. examined electrodeposited Ni−Fe catalysts in a mixed oxide system for their oxygen evolution capability.[20] These electro-deposited films showed higher oxygen evolution activity compared to that of pure Ni or Fe oxide. Miller also investigated a mixed Ni−Fe oxide system by reactively sputtering films of Ni−Fe onto a support and noted a similar increase in activity.[10] Finally, Trasatti et al. have extensively examined various mixed oxide systems including mixed Ni−Fe oxide catalysts prepared by dip-coating over Ni and Fe supports. They have also reported the synergistic effect of the mixed oxide over pure nickel or iron oxide with compositions ranging from 10 to 20 mol % FeO_x showing the highest activity.[34−36] Tafel analysis was conducted in these experiments to help explain the increase in activity which showed decreases in the Tafel slope with increasing Fe content.

These reports have shown the benefits of mixed oxide surfaces, particularly Ni−Fe mixed oxides, toward oxygen evolution, and a range where the optimal composition of $(Fe,Ni)O_x$ has been targeted. However, a detailed spectroscopic characterization of the catalyst surface was not reported which would provide valuable information regarding why the surface was more active. High surface area catalyst synthesis processes used to easily tailor bulk catalyst compositions were also not applied. Thus, there remain outstanding questions about the mechanism for improved activity, and answers to those questions could lead to new materials with better oxygen evolution activity.

To help respond to these remaining questions, mixed Ni−Fe oxide electrocatalysts have been synthesized using an evaporation-induced self-assembly (EISA) synthesis process, a hard templating process, and a dip-coating process to provide electrocatalysts with varying surface areas. Electrocatalysts were physically characterized by X-ray diffraction (XRD) and Brunauer−Emmett−Teller (BET) surface analysis. Spectrosco-py techniques including temperature programmed reaction spectroscopy (TPRS), and X-ray photoelectron spectroscopy (XPS) have been used to investigate the electrocatalyst surface compositions, and catalysts were electrochemically character-ized using cyclic voltammetry and chronoamperometry. Raman spectroscopy, in situ X-ray absorption near edge structure (XANES), and extended X-ray absorption fine structure (EXAFS) experiments were used to help identify the mechanisms for the improved activity seen in the mixed metal oxide electrocatalysts. The detailed spectroscopy methods used here to examine both the catalyst surface and bulk composition will give further information about the factors responsible for the increase in activity toward oxygen evolution for these mixed Ni−Fe oxides.

■ METHODS

Catalyst Synthesis. Three synthesis methods were used to create mixed Ni−Fe oxide catalysts including evaporation-induced self-assembly (EISA),[37] hard templating,[38] and a dip coating of a Ni mesh.[39,40]

Evaporation-Induced Self-Assembly (EISA). Catalysts were synthesized using an EISA technique to alter bulk catalyst composition.[37] One gram of P123 surfactant was dissolved into a mixture composed of 5 g of deionized water and 5 g of ACS grade ethanol. Subsequently, metal nitrate precursor salts were dissolved into this mixture in the desired molar compositions for the final catalyst powder. This solution was then transferred to a ceramic boat and heated in air using a controlled procedure. First, the solution was heated to 120 °C and held for 12.5 h. This temperature was used to remove any water and residual ethanol. Next, the resulting gel was slowly ramped to 350 at 1 °C/min and held at 350 °C for 4 h. This step was intended to remove the P123 surfactant while maintaining a high surface area framework. Finally, the remaining material was heated to 550 at 1 °C/min and held for 4 h. The resulting material was then ground using a mortar and pestle and stored for characterization. The mol % of Fe in each sample was computed as mol % = $mol_{Fe}/(mol_{Fe} + mol_{Ni}) \times 100$.

Synthesis of the Hard Template (SBA-15). The hard template synthesis was carried out similar to the work of Wang et al.[38] The procedure is as follows: 5.68 g of P123 and 14.4 g of NaCl were dissolved in 160 mL of 1.0 M HCl aqueous solution, and the mixture was stirred at 35 °C for 6 h. A mixture of tetraethoxysilane, TEOS, (42.56 mmol, 8.87 g), and triethoxyvinylsilane, TEVS, (10.64 mmol, 2.02 g) was added slowly to the obtained solution under stirring. After stirring for 4 h at 35 °C, the obtained suspension was aged for 24 h at 100 °C under static conditions in a polypropylene bottle. The product was filtered and washed with deionized water, ethanol, and acetone five times in the mentioned order, and then dried at 100 °C overnight. Finally, P123 was removed by overnight treatment with 60 wt % H_2SO_4. The product was filtered and washed again with deionized water, ethanol, and acetone. The H_2SO_4 treatment was repeated for three consecutive nights, and the final product was dried overnight after the rigorous washing procedure.

Synthesis of Mixed Ni−Fe Oxides over the Hard Template. The nanocasting procedure that was followed is similar to that of Wang et al.[38] except for using citrate complexes as the precursor. The precursor was prepared by dissolving the desired molar ratio of nickel nitrate and iron nitrate in a mixed solution of deionized water and ethanol, and citric acid where the molar ratio of citric acid to metal ions was 1:1. Typically, a total of 8 mmol of metal nitrate salts in the desired metal molar ratio and 8 mmol of citric acid were dissolved in a mixture of 15 mL of ethanol and 5 mL of deionized water. The mixture was stirred at room temperature overnight. A 1.0 g portion of the hard template was added to the homogeneous solution, and the mixture was stirred for 6 h more at 40 °C until it became viscous. The obtained viscous solution was dried at 80 °C for 6 h, then calcined at 550 °C for 4 h in air to decompose the nitrate species. After grinding the resulting material by hand in a mortar and pestle, the following washing procedure was used. The material was washed with deionized water, ethanol, and acetone. Then, the silica framework was dissolved away by a 2 M NaOH aqueous solution at room temperature three times. The final product was washed with water, ethanol, and acetone and dried at 100 °C overnight. This procedure was followed to synthesize pure nickel oxide and 3%, 5%, 15%, 20% mixed Ni−Fe oxides as well as iron oxide.

Mixed Ni−Fe Coated Mesh Electrodes. The catalyst was deposited by dipping a Ni mesh, acquired from Dexmet Corp., into a precursor solution and thermally decomposing the precursor into the desired metal oxides.[39,40] The precursor

solutions were 0.2 M $Ni(NO_3)_2 \cdot 6H_2O$, and 0.2 M $Fe(NO_3)_3 \cdot 9H_2O$, each dissolved in deionized water, and mixed according to the desired metal molar amounts. To ensure good adhesion of the catalyst precursor to the mesh, the mesh was first chemically etched using concentrated H_2SO_4. After thoroughly rinsing the etched mesh with deionized water, it was then dried and weighed prior to dipping. The mesh was dipped into the precursor solution and subsequently dried at 120 °C until the desired mass has been deposited, approximately 1 mg/cm^2 (geometric area of 1 cm ×1 cm). The coated mesh was then heated in air at 300 °C for 24 h to decompose the metal salts into the desired metal oxides. The resulting mesh was then weighed, sonicated in water to remove excess salts and easily detachable oxide scale that may still be on the surface, dried for 30 min at 120 °C, and then weighed again to determine electrocatalyst loading prior to electrochemical testing.

Catalyst Characterization. Catalyst crystallinity and structure was examined using a Rigaku Theta-Theta Diffractometer equipped with a Cu detector and an incident beam wavelength of 1.542 Å. The beam energy was set to 30 eV and beam current to 30 mA. Catalyst surface area was examined using the BET method with a Nova 2200 Surface Area Analyzer. Catalyst morphology and surface composition were investigated using a Philips XL30 Scanning Electron Microscope with Energy Dispersive X-ray Spectroscopy (SEM/EDS). Surface composition measurements were carried out by X-ray Photoelectron Spectroscopy (XPS) with an Al source. The Raman spectra of the mixed oxides were obtained with a high resolution, dispersive Raman spectrometer system (Horiba-Jobin Yvon LabRam HR) equipped with three laser excitations (532, 442, and 325 nm). The lasers were focused on the samples with a confocal microscope equipped with a 50X long working distance objective (Olympus BX-30- LWD) for the visible lasers. The catalyst samples, typically consisting of between 5 and 10 mg of loose powder, were placed on a glass slide underneath the objective. The Raman spectra were collected with the 442 nm laser to avoid iron oxide fluorescence typically encountered using a 532 nm laser. For the acquisition of the Raman spectra, the accumulation was collected at 60 s/scan for 5 scans with a 500 μm opening for the laser light. X-ray absorption spectroscopy experiments were carried out at Brookhaven National Laboratory's National Synchrotron Light Source on beamline X19A. In situ electrochemical experiments were performed in a custom built cell that enables both transmission and fluorescence measurements.[41]

Temperature Programmed Reaction Spectroscopy. Temperature programmed surface reaction experiments using methanol[42] were carried out using an Altamira Instruments system (AMI 200) reactor and Dymaxion Dycor mass spectrometer (DME200MS). Typically about ~200 mg of catalyst was loaded into a U-tube sample holder in an Altamira Instruments System (AMI-200). The catalysts were pretreated by oxidation in flowing O_2/He at 350 °C for 45 min to dry the powders and to remove easily oxidizable impurities. Methanol was chemisorbed on the catalysts at 100 °C from a 2000 ppm CH_3OH in He gas stream for 30 min, the gas stream was switched to He for 30 min to desorb any physically adsorbed methanol, and the temperature was increased at a rate of 10 °C/min to 400 °C in the flowing He stream. The reaction products were analyzed with an online mass spectrometer (Dymaxion Dycor, DME200MS). The execution of the experiment, as well as the collection of data, was automatically done by the "Dycor System 200" software after the procedure was programmed. The mass spectrometer data were normalized by dividing the mass spec signal intensity by the total area of the sample (total area = BET surface area × sample mass), giving units of Intensity/m^2.

Electrocatalytic Activity. Catalyst inks were formed by combining 20 mg of EISA or hard-templated catalyst powder, 645 mg of 5 wt % AS4 ionomer solution from Tokuyama Corp., 200 μL of deionized water, and 800 μL of isopropanol. This solution was sonicated for 60 min. Next, the catalyst ink was painted on to a piece of Toray TGPH-060 carbon paper with 1 cm ×2 cm dimensions and heated at 120 °C for 10 min to remove any water or alcohol from the surface. This process was repeated until a loading of approximately 0.5 mg/cm^2 was achieved in all cases, and the results have been normalized by the actual catalyst mass loading. Electrochemical experiments were performed with a Gamry Reference 600 potentiostat. A Pt wire counter electrode and Hg/HgO reference electrode were used throughout these experiments. 1 M KOH was used as the electrolyte which was deaerated with pure argon for 30 min prior to each experiment. Initialization of the catalyst was carried out in an oxygen evolution region at a potential of 0.742 V vs Hg/HgO for a period of 3 h. Polarization curves were examined using a scan rate of 1 mV/s between 0.6 and 0.7 V vs Hg/HgO and used in Tafel analysis. Steady-state catalytic activity was subsequently examined at potentials between 0.542 to 1.042 V vs Hg/HgO in 50 mV increments for 20 min at a time. All results have been normalized by a reference electrode potential which was measured versus a second, dedicated electrode before each experiment. The overpotential, η, was determined using eq 1.

$$\eta = E_{applied} - E^\circ + E_{ref} \tag{1}$$

$E_{applied}$ is the applied potential with E° and E_{ref} being the equilibrium reaction potential and reference electrode potential, respectively. E° is pH dependent and was calculated accordingly for the pH in each experiment with the formula shown in eq 2.

$$E^\circ = 0.401 + 0.059(14 - pH) \tag{2}$$

All results involving electrocatalytic activity have been reported as current vs overpotential unless otherwise noted.

■ RESULTS AND DISCUSSION

Mixed Ni−Fe Oxide Electrocatalytic Activity. Mixed Ni−Fe oxide electrodes were tested for their oxygen evolution activity to determine the most active composition of these mixed catalysts for those created through the EISA synthesis process as well as a hard-templating process, and dip-coating method. After initialization of the catalyst surface, polarization data was taken at 1 mV/s between 0.6 and 0.7 V vs Hg/HgO and is shown for the EISA synthesized electrocatalysts in Figure 1. Ten mol % Fe catalysts showed the highest activity of the electrocatalysts examined, similar to results produced by Krstajić and Trasatti.[36] Tafel analysis was conducted and is included in the Supporting Information, with Tafel slopes decreasing from greater than 50 mV/dec to 40 mV/dec for the Ni−Fe mixed oxides.

After examining polarization activity of the mixed oxides, steady-state activity of each electrode was tested at potentials ranging from 0.542 to 1.042 V vs Hg/HgO in 50 mV intervals for a period of 20 min at each potential. The steady state
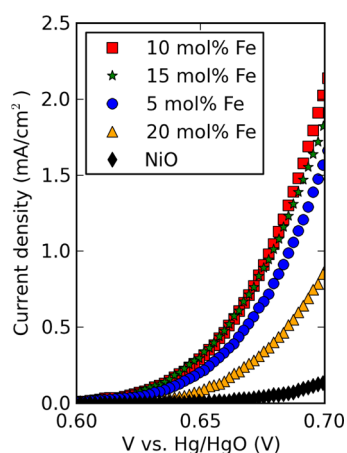
Figure 1. Geometric area-normalized polarization (scan rate = 1 mV/s) data of mixed Ni−Fe oxide catalysts (synthesized by the EISA method) showing the highest activity for 10 mol % Fe oxide. The equilibrium potential for O_2 evolution is approximately 0.308 V vs Hg/HgO.

current at the end of this time period was recorded for that overpotential. All results have been normalized by the catalyst mass unless otherwise noted. Figure 2 shows the current
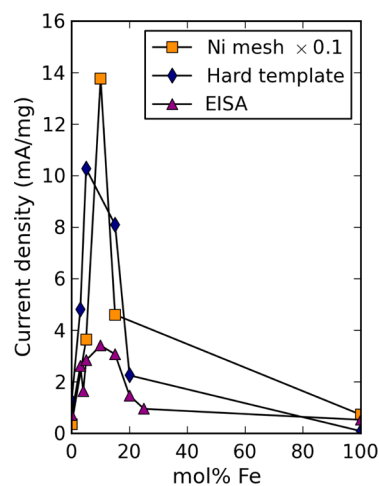

Figure 2. Electrochemical oxygen evolution activity at a fixed overpotential of 360 mV for the varying synthesis methods and compositions of mixed metal oxide electrocatalysts.

density at a fixed overpotential of approximately 360 mV corresponding to approximately 0.668 V vs Hg/HgO depending on the exact pH as a function of the bulk Fe content (in mol %) for the three different synthesis methods. This overpotential was chosen as it reflects the onset of practical current density. A peak in catalytic activity is observed near 10 mol % Fe for all three synthesis methods. As Fe content is increased beyond 10 mol %, catalytic activity starts to decrease, similar to the results shown in the polarization data. These results are also similar to literature results,[10,34,43] and show that the enhanced activity is practically independent of the synthesis method. The dip-coated mesh electrodes were more active by an order of magnitude than either the EISA or hard-template synthesized electrocatalysts. We hypothesize the mesh may be substantially better because of the direct electrical contact of the oxide with the conductive metal mesh, and the lack of

ionomer and other ink components that could block some surface sites.

The BET surface area was measured for all of these catalysts, and when the catalytic activity is plotted after being normalized by these values, the same trend is observed (not shown). Since the trends are practically independent of the synthesis method, for the remainder of the paper we focus on the results for the EISA synthesis.

Catalyst surface areas for each catalyst synthesized using the EISA process are shown in Table 1. The surface areas for these

Table 1. BET Surface Areas for Mixed Ni−Fe Oxide Catalysts Produced by the EISA Method

catalyst	surface area (m^2/g)
NiO	14
3 mol % Fe	18
4 mol % Fe	19
5 mol % Fe	19
10 mol % Fe	18
15 mol % Fe	26
20 mol % Fe	31
Fe_2O_3	13

catalysts ranged from 13 to 31 m^2/g. We conclude that the enhanced oxygen evolution activity cannot be explained by variations in electrocatalyst surface area, and that there must be an intrinsic increase in the surface activity for the mixed oxide samples near 10 mol % Fe.

Physical Characterization. The electrocatalyst powders resulting from the EISA synthesis were examined using XRD. The bulk crystal structure of each electrocatalyst synthesized by the EISA method was determined by XRD (Figure 3). As the
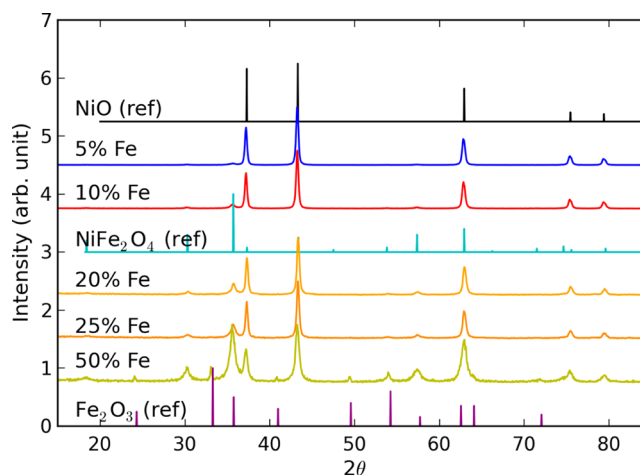

Figure 3. XRD patterns of the 5, 10, 20, 25, and 50 mol % Fe mixed samples. Lattice constants for NiO and all mixed Ni−Fe oxides were found to be 4.18 Å, suggesting Fe was not substitutionally incorporated into the NiO lattice. The formation of $NiFe_2O_4$ and Fe_2O_3 phases are observed as the concentration of Fe increases.

Fe content is increased up to 10 mol %, the peak positions from the NiO lattice remain constant. The lattice constants from each of these XRD patterns, excluding pure iron oxide, yielded a value of 4.18 Å. This suggests Fe was not substitutionally incorporated into the NiO lattice as the lattice constant would have changed with Fe composition. These observations are consistent with literature reports of the oxidation of Ni−Fe

alloys in this composition range, where an internal NiO scale forms with an outer shell of Fe−Ni spinel oxide and Fe_2O_3.[44] In other reports, Fe has very limited solubility in the NiO lattice at high Ni concentrations under the low calcination conditions we prepared the electrocatalysts under.[45] The solubility of Fe in NiO at 1200 °C was computed to be less than 6%;[45] our calcination temperature was only 550 °C, where the solubility is much lower. We did not heat our powders to such high temperatures to avoid loss of surface area. There is a small peak in the XRD spectra at $2\theta \approx 35°$ that grows as the concentration of Fe is increased. This peak is due to the formation of the $NiFe_2O_4$ spinel phase. The peak intensity for the spinel phase increases with increasing Fe content up to 25 mol % Fe. At higher Fe compositions, peaks associated with Fe_2O_3 begin to be observed, which continue to grow with increasing Fe composition.

The formation of the spinel phase could be a contributing factor to the enhanced activity. The related $NiCo_2O_4$ spinel phase is known to be a good oxygen evolution electrocatalyst, and it is known to be promoted by Fe oxides.[34] Furthermore, spinels have been used for hydrogen production from water in solar thermal approaches.[46,47] We observed increasing peak intensity associated with the spinel phase in the XRD up through 25 mol % Fe before the obvious formation of Fe_2O_3 starts to occur. However, the enhancement effect of adding Fe begins to decrease between 10 and 15 mol % Fe, and is practically gone by 20 mol % Fe. The oxygen evolution activity is sensitive to the near surface composition. Perhaps at increasing Fe concentrations very thin films of an (possibly amorphous) oxide like Fe_2O_3 could form which effectively poison the surface, even though they are not detectable by XRD until much higher Fe concentrations.

Raman spectroscopy is a great complement to XRD since, unlike XRD, it can also detect crystalline nanoparticles smaller <4 nm and amorphous phases that cannot be detected by XRD.[48] Raman spectroscopy was utilized to investigate the oxide phases present in the 5, 10, and 20% EISA powders, and the spectra are presented in Figure 4 with that of the bulk NiO reference. The main NiO band at 1101 cm^{-1} is present in all the samples indicating that the bulk NiO phase is retained upon Fe addition, in agreement with XRD data. The weaker NiO Raman band at 900 cm^{-1}, however, is lost at concentrations
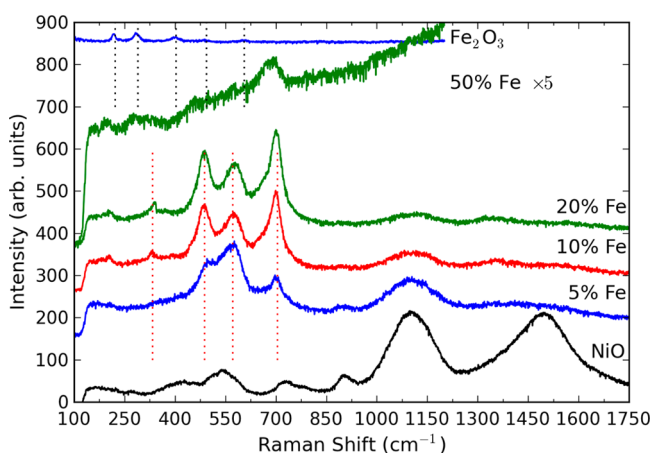
greater than 5 mol % Fe. The 5 mol % Fe sample also exhibits 3 new Raman bands at 483, 574, and 703 cm^{-1} indicative of a $NiFe_2O_4$ spinel phase.[49−51] At 10 and 20 mol % Fe, two additional weak Raman bands from the $NiFe_2O_4$ phase appear at 207 and 335 cm^{-1}. Given that both Raman and XRD detect the $NiFe_2O_4$ phase at 5 mol % Fe indicates its presence in the bulk phase of the Fe−Ni mixed oxide. Considering the low intensity of the $NiFe_2O_4$ peaks in XRD at 5 mol % Fe and the high intensity of the peaks in Raman, the $NiFe_2O_4$ phase may be present as small nanoparticles at concentrations <5 mol % Fe.

It is critical to note that the presence of separate Fe oxide phases is not detected by Raman spectroscopy at concentrations up to 20 mol % Fe. Since Raman is extremely sensitive to small Fe oxide nanoparticles, the absence of Raman bands from iron oxide phases, especially the strong bands from α-Fe_2O_3, suggest that this phase is probably not present in significant concentrations.[52]

SEM/EDS experiments were performed to examine the distribution of Fe and Ni in the mixed oxide samples at a macroscale. Mixed Ni−Fe oxide powders were applied to a carbon paper support as described previously using a catalyst ink. SEM images were taken at 1 and 5 μm resolutions, and elemental mapping using EDS was conducted. Shown in Figure 5 is an SEM image of a 5 mol % Fe mixed Ni−Fe catalyst surface on a carbon paper support with both 1 and 5 μm scales and elemental mappings of the Ni and Fe locations on the surface. From the SEM/EDS images, it was seen that Ni and Fe are basically uniformly distributed across the catalyst surface. Even if Fe is not incorporated in the NiO lattice, there exists a close proximity between both Ni and Fe at the length scale probed by SEM. There do exist places on the catalyst surface where Fe has locally higher concentrations, one of which is circled in red. This region was above average at a concentration of about 30 mol % Fe. Even with this higher concentration of Fe, there is no evidence from either XRD or Raman of large crystalline phases of Fe oxide forming.

Surface Characterization of Mixed Ni−Fe Oxides. XPS was used to investigate the surface phases for five of Ni−Fe oxide powders which were previously examined, including NiO, 5, 10, and 20 mol % Fe mixed Ni−Fe oxides, and Fe_2O_3. The Ni XPS spectra for the four samples containing Ni are shown in Figure 6. Evident in all four of the Ni containing oxides are characteristic peaks for NiO including the $2p_{1/2}$ and $2p_{3/2}$ peaks, at 854 and 873 eV, respectively. All of these oxides appear to have similar phases of NiO present. There is no quantifiable chemical shift in the binding energy for any of these oxides which is consistent with a lack of bulk alloying in these oxides. Peaks in the pure NiO sample appear sharper than in the mixed oxide, although it not clear why that is the case.

The Fe XPS results are shown in Figure 7. The Fe oxide signals obtained in these experiments are quite low, especially in the case of the mixed oxide samples. Fe_2O_3 has two characteristic peaks corresponding to binding energies of approximately 711 and 724 eV with shakeup satellite features at 719 and 732 eV. These peaks can be differentiated in the pure phase Fe_2O_3 sample with the shakeup satellite features at 719 and 732 eV having rather low signals, but it is not possible to conclusively identify the shakeup satellite features in any of the mixed oxide samples because of low signal intensity. Argon sputtering of the catalyst surface was carried out to determine if any differences in the surface versus bulk composition could be
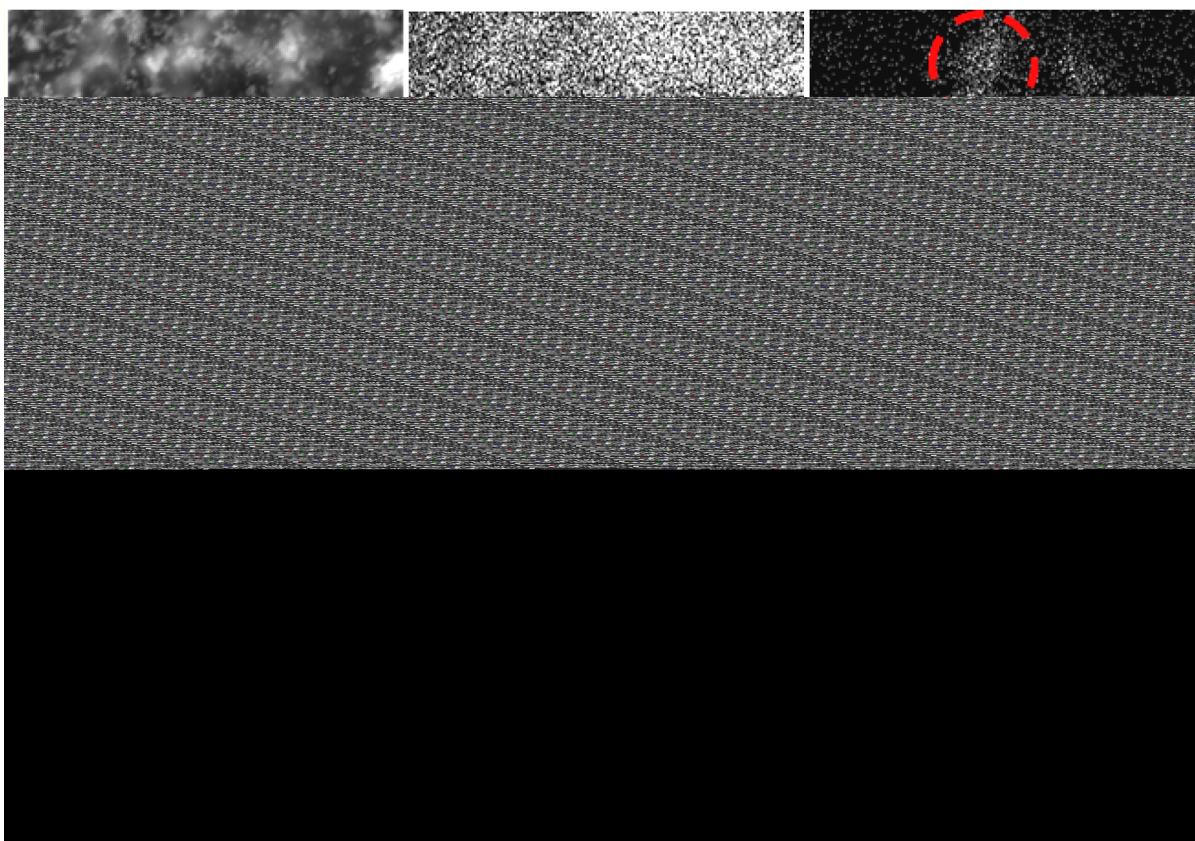

Figure 4. Ambient Raman spectra of some Ni−Fe powders prepared by the EISA method. The dashed black lines are reference spectra for α-Fe_2O_3 at 221, 289, 403, 493, and 605 cm^{-1}.[52] The dashed red lines are reference peaks for $NiFe_2O_4$ at 333, 487, 571, and 704 cm^{-1}.[49,50]

Figure 5. One micrometer and 5 μm SEM images of a 5 mol % Fe mixed Ni−Fe catalyst along with elemental mapping of the surface for Ni and Fe. Particle sizes ranged from under a micrometer to a few micrometers. Ni and Fe sites were located across the catalyst surface with some locally higher concentrations. Circled in red is an area of concentrated Fe.
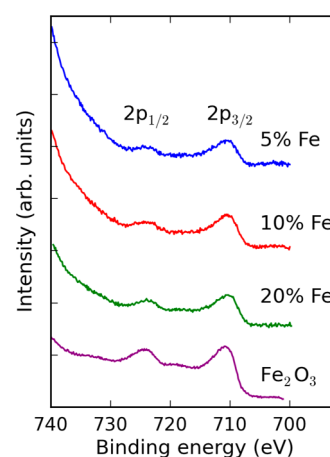

Figure 7. Fe XPS spectra from pure Fe_2O_3 and 5, 10, and 20 mol % Fe-mixed Ni−Fe oxides. The pure iron oxide (Fe_2O_3) sample contains two major peaks at 711 and 724 eV and two shakeup satellite features at 719 and 732 eV. The Fe-containing samples contain 2 peaks that are consistent with the Fe_2O_3 reference spectra.

Figure 6. Ni XPS spectra taken from pure NiO and 5, 10, and 20 mol % Fe-mixed Ni−Fe oxides. All of these samples have characteristic NiO peaks for both the $2p_{1/2}$ and $2p_{3/2}$ features.

seen, but no quantifiable differences were found suggesting the surface composition was similar to the bulk composition.

X-ray absorption spectroscopy analysis was conducted on the oxide powders in air to determine the oxidation state of Fe in the 10 mol % mixed oxide sample. The Fe K-edge XANES data are shown in Figure 8 showing the signal from the 10 mol % mixed oxide sample as well as three reference samples of FeO, Fe_3O_4, and $α$-Fe_2O_3. The 10 mol % sample spectrum shares features of the Fe_3O_4 and Fe_2O_3 spectra, suggesting that the Fe

oxidation state in the mixed oxide phase is predominantly Fe^{3+} and that sample contains some Fe atoms in a tetrahedral environment. The key feature in common with Fe_3O_4 is the pre-edge peak at 7115 eV in the 1s-3d transition region, which is a signature of tetrahedrally coordinated Fe as found in Fe_3O_4 but not in $α$-Fe_2O_3. The second feature is the position of the main edge corresponding to the 1s-4p transition. The absorption edge energy is very sensitive to the oxidation state
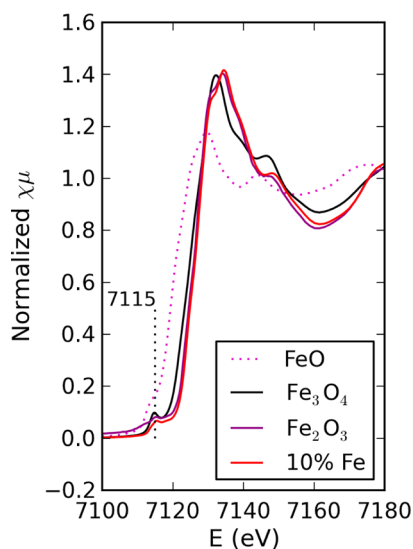
Figure 8. XANES analysis of the Fe K-edge of the mixed oxide sample containing 10 mol % Fe and several reference iron oxides.

of transition metal ions, and it is shifted to lower energies in Fe_3O_4 (Figure 8) because of a more reduced state of Fe (caused by the submixture of Fe^{2+}) compared to that in α-Fe_2O_3, which is purely Fe^{3+}. Since the main absorption edge of the 10 mol % sample is most similar to that of the α-Fe_2O_3 reference, our interpretation of these results is that there are only Fe^{3+} ions in the 10% Fe sample, and some of them are tetrahedrally coordinated. There may also be disperse phases of α- and/or γ-Fe_2O_3 present, even though they do not appear in the XRD spectra, nor are they readily apparent in the Raman spectra, although the XPS spectra are consistent with the presence of Fe_2O_3.

In situ EXAFS experiments on the Fe and Ni K-edges were conducted on the 10 mol % Fe mixed oxide powder in air, under open-circuit conditions in electrolyte and under electrochemical oxygen evolution conditions. The results in air are similar to previously reported EXAFS spectra of $NiFe_2O_4$.[53] The Ni K-edge EXAFS showed virtually no change in the peak intensities in the mixed oxide sample under oxygen evolution reaction conditions (Figure 9). We would expect a change could occur because of changes in Ni−O coordination as a result of oxygen containing adsorbates during the oxygen evolution reaction or from significant changes in the oxidation state of the Ni atoms. It is possible that since EXAFS is a bulk technique, and the sample is predominantly Ni−O in composition that changes in the spectrum were undetectable because of the large bulk to surface volume ratio. Unlike the Ni K-edge, however, the Fe K-edge spectrum shows some changes under reaction conditions. The intensity of the peak associated with Fe−O coordination increases in intensity, and the relative intensities of the peaks associated with the Fe^{oct}-Ni/Fe^{oct} and Fe^{oct}-Fe^{tet} coordination shells change under OER conditions. This change is indicative of further coordination of Fe atoms under oxygen evolution conditions and suggests that Fe are certainly affected by the reaction conditions, and that they could be involved during this reaction process.

Fe^{3+} atoms are present in both tetrahedral and octahedral sites in the $NiFe_2O_4$ inverse spinel structure.[54,55] Increased coordination of Fe atoms could indicate the movement of Fe atoms from tetrahedral positions to open octahedral sites within the spinel structure, with higher occupation of
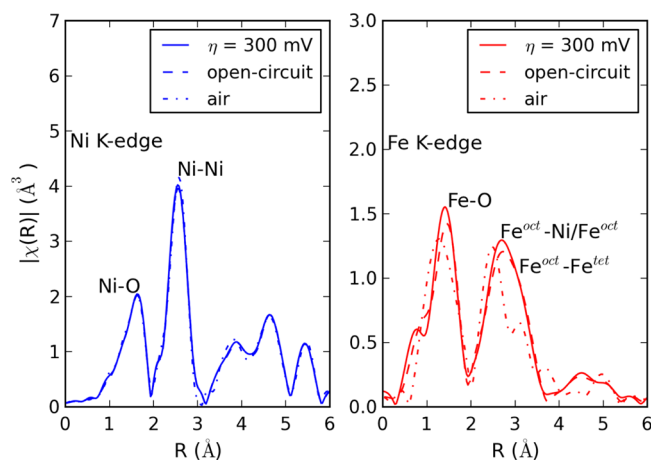
octahedral sites being found in nanophase $NiFe_2O_4$ materials previously.[55,56] Another mechanism resulting in increased Fe coordination could be the formation of Fe_2O_3 phases under these oxidizing conditions. It seems unlikely this occurs, as Fe_2O_3 is known to be a poor electrocatalyst for the oxygen evolution reaction, and this mechanism is expected to deactivate the surface, which was not observed; constant, steady-state currents were observed with these electrocatalysts over the course of the experiments.

Temperature Programmed Reaction Spectroscopy (TPRS). The surface chemistry of the Fe−Ni oxide electrocatalysts was chemically probed with CH_3OH-TPRS spectroscopy because of the sensitivity of this probe molecule to the nature of oxide surface sites.[57] The results for CO_2 (a characteristic product on basic sites) and methanol desorption are presented below in Figure 10 (all results for all species detected are available in the Supporting Information).
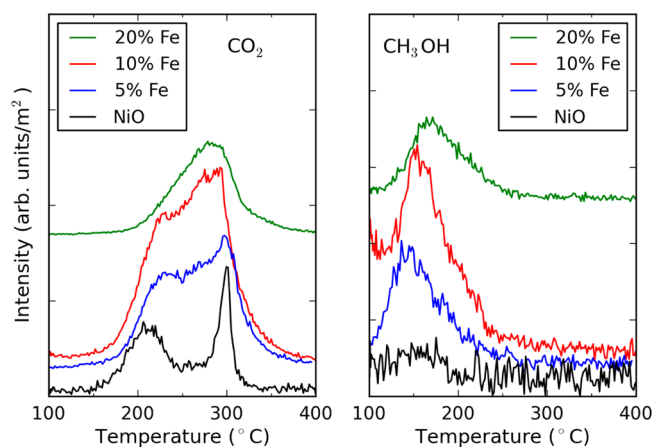

Figure 9. Fourier transform magnitudes of k^2-weighted EXAFS data for the Ni and Fe K-edge of the 10 mol % Fe mixed Ni−Fe oxide catalyst in air, under open circuit conditions in alkaline electrolyte, and at an overpotential of 300 mV under oxygen evolution conditions.

**Figure 10.** CH_3OH-TPRS of Ni−Fe mixed oxide powders.

The main desorption products from NiO were CO and CO_2 with minor amounts of CH_3OH and HCHO, indicating that the surface primarily consists of basic active sites.[57] In contrast, the primary desorption products from α-Fe_2O_3 (not shown here) are dimethyl ether (DME) and CH_3OH with a minor amount of HCHO.[42] The significant formation of DME reflects

the acidic nature of the active sites on the surface of α-Fe$_2$O$_3$ with HCHO being formed on a small number of surface redox sites.[42] No DME desorption was observed on NiO or the mixed-metal Ni−Fe oxides examined in this work, suggesting there is no bulk-like Fe$_2$O$_3$ formation at the surface. The addition of 5 mol % Fe sample shows increased amounts of CO and CO$_2$ desorption products reflecting the basic character of this surface, and an increase in the number of basic sites. At the same time, some methanol is observed to desorb, indicating Fe-containing sites are present on the surface. The 10 mol % Fe sample exhibits a further increase in CO$_2$ production indicating a greater number of basic surface sites. The 20 mol % Fe sample, shows a decrease in the production of CO$_2$, suggesting fewer basic surface sites.

The predominance of CO$_2$ formation during the CH$_3$OH-TPRS experiments on the Fe−Ni oxides suggests that these surfaces primarily consist of basic character sites similar to NiO. The number of basic sites (based on the area under the CO$_2$ desorption curves) on the Ni−Fe oxides follows the trend

$$NiO \leq 20\%Fe < 5\%Fe < 10\%Fe$$
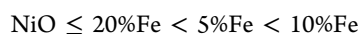
which parallels the oxygen evolution activity trend

$$NiO < 20\%Fe < 5\%Fe < 10\%Fe$$
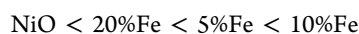
This suggests that maximizing the number of basic sites on the Fe−Ni oxide catalyst surface may be an important parameter for enhancing electrochemical oxygen evolution activity. On the basis of the characterization presented above, it seems likely that NiFe$_2$O$_4$ may be a contributing bulk phase to the number of basic sites.

CONCLUSIONS

Mixed Ni−Fe oxide catalysts were synthesized using an evaporation-induced self-assembly process and characterized using XRD, Raman spectroscopy, BET, SEM/EDS, XPS, XANES, XAS, CH$_3$OH-TPRS, and electrochemical methods. The mixed Ni−Fe oxide catalysts showed much higher activity toward oxygen evolution and methanol oxidation than either of the pure oxides with a peak in activity occurring near 10 mol % Fe. A similar trend in activity versus catalyst composition was shown for electrocatalysts synthesized by hard templating and dip-coating.

XRD and Raman conclusively identified the formation of a spinel NiFe$_2$O$_4$ phase in coexistence with NiO at low Fe concentrations, and the formation of Fe$_2$O$_3$ at higher concentrations was observed by XRD. The primary oxidation state of the Fe in the mixed oxide was identified using XANES analysis and found to be +3, consistent with the formal charges of Fe in a NiFe$_2$O$_4$ or Fe$_2$O$_3$ phase. EXAFS showed that the average coordination of Fe atoms increases under oxygen evolution conditions possibly because of an increase in octahedrally coordinated Fe in NiFe$_2$O$_4$. This indicates that Fe may be involved in enhancing oxygen evolution and that Fe could be in the active site for oxygen evolution on the mixed metal oxide electrocatalysts. Since Fe^{3+} in Fe$_2$O$_3$ is not a very good electrocatalyst, NiFe$_2$O$_4$ is implicated as a contributing phase to improving the oxygen evolution activity. CH$_3$OH-TPRS has shown that the mixed oxide surface basicity follows the same trend as oxygen evolution activity, suggesting the importance of basic active sites for electrochemical oxygen evolution.

ASSOCIATED CONTENT

⑤ Supporting Information

Figures containing all of the products from the CH$_3$OH-TPSR studies on each surface, as well as additional electrochemical characterization of the electrocatalysts. This material is available free of charge via the Internet at http://pubs.acs.org.

AUTHOR INFORMATION

Corresponding Author
*E-mail: jkitchin@andrew.cmu.edu.

Notes
The authors declare no competing financial interest.

REFERENCES

(1) Nørskov, J. K.; Bligaard, T.; Logadottir, A.; Kitchin, J. R.; Chen, J. G.; Pandelov, S. *J. Electrochem. Soc.* **2005**, *152*, J23.
(2) Dau, H.; Limberg, C.; Reier, T.; Risch, M.; Roggan, S.; Strasser, P. *ChemCatChem* **2010**, *2*, 724.
(3) Man, I. C.; Su, H.-Y.; Calle-Vallejo, F.; Hansen, H. A.; Martínez, J. I.; Inoglu, N. G.; Kitchin, J.; Jaramillo, T. F.; Nørskov, J. K.; Rossmeisl, J. *ChemCatChem* **2011**, *3*, 1159.
(4) Kanan, M. W.; Nocera, D. G. *Science* **2008**, *321*, 1072.
(5) Kanan, M. W.; Surendranath, Y.; Nocera, D. G. *Chem. Soc. Rev.* **2009**, *38*, 109.
(6) Lutterman, D. A.; Surendranath, Y.; Nocera, D. G. *J. Am. Chem. Soc.* **2009**, *131*, 3838.
(7) Hansen, H. A.; Rossmeisl, J.; Nørskov, J. K. *Phys. Chem. Chem. Phys.* **2008**, *10*, 3722.
(8) Trasatti, S.; Lodi, G. *Electrodes of Conductive Metallic Oxides, Part A and Part B*; Elsevier: Amsterdam, The Netherlands, 1980 and 1981.
(9) Singh, R. N.; Madhu; Awasthi, R.; Sinha, A. S. K. *Electrochim. Acta* **2009**, *54*, 3020.
(10) Miller, E. L.; Rocheleau, R. E. *J. Electrochem. Soc.* **1997**, *144*, 3072.
(11) Singh, R. N.; Hamdani, M.; Koenig, J. F.; Poillerat, G.; Gautier, J. L.; Chartier, P. *J. Appl. Electrochem.* **1990**, *20*, 442.
(12) Sequeira, C. A. C.; Santos, D. M. F.; Cameron, E.; Brito, P. S. D. *Mater. Technol.* **2008**, *23*, 142.
(13) Wang, X.; Luo, H.; Yang, H.; Sebastian, P. J.; Gamboa, S. A. *Int. J. Hydrogen Energy* **2004**, *29*, 967.
(14) Tunold, R.; Marshall, A. T.; Rasten, E.; Tsypkin, M.; Owe, L.-E.; Sunde, S. *ECS Trans.* **2010**, *25*, 103.
(15) Marshall, A. T.; Sunde, S.; Tsypkin, M.; Tunold, R. *Int. J. Hydrogen Energy* **2007**, *32*, 2320.
(16) Miao, H. J.; Piron, D. L. *Can. J. Chem. Eng.* **1993**, *71*, 564.
(17) Lyons, M. E. G.; Brandon, M. P. *J. Electroanal. Chem.* **2010**, *641*, 119.
(18) Man, I. C.; Su, H.-Y.; Calle-Vallejo, F.; Hansen, H. A.; Martínez, J. I.; Inoglu, N. G.; Kitchin, J.; Jaramillo, T. F.; Nørskov, J. K.; Rossmeisl, J. *ChemCatChem* **2011**, *3*, 1159.

(19) Trasatti, S. In *Electrochemical hydrogen technologies*; Wendt, H., Ed.; Elsevier: Amsterdam, The Netherlands, 1990; p 104.

(20) Corrigan, D. A. *J. Electrochem. Soc.* **1987**, *134*, 377.

(21) Forgie, R.; Bugosh, G.; Neyerlin, K. C.; Liu, Z.; Strasser, P. *Electrochem. Solid-State Lett.* **2010**, *13*, B36.

(22) Snook, G. A.; Duffy, N. W.; Pandolfo, A. G. *J. Power Sources* **2007**, *168*, 513.

(23) Kibria, M. F.; Mridha, M. S. *Int. J. Hydrogen Energy* **1996**, *21*, 179.

(24) Kleiman-Shwarsctein, A.; Hu, Y.-S.; Stucky, G. D.; McFarland, E. W. *Electrochem. Commun.* **2009**, *11*, 1150.

(25) Merrill, M. D.; Dougherty, R. C. *J. Phys. Chem. C* **2008**, *112*, 3655.

(26) Trasatti, S. *Electrochim. Acta* **1984**, *29*, 1503.

(27) De Faria, L. A.; Prestat, M.; Koenig, J. F.; Chartier, P.; Trasatti, S. *Electrochim. Acta* **1998**, *44*, 1481.

(28) Bockris, J. O. M.; Otagawa, T. *J. Electrochem. Soc.* **1984**, *131*, 290.

(29) Suntivich, J.; May, K. J.; Gasteiger, H. A.; Goodenough, J. B.; Shao-Horn, Y. *Science* **2011**, *334*, 1383.

(30) Jörissen, L. *J. Power Sources* **2006**, *155*, 23.

(31) Esswein, A. J.; McMurdo, M. J.; Ross, P. N.; Bell, A. T.; Tilley, T. D. *J. Phys. Chem. C* **2009**, *113*, 15068.

(32) Zhao, Y.; Hernandez-Pagan, E. A.; Vargas-Barbosa, N. M.; Dysart, J. L.; Mallouk, T. E. *J. Phys. Chem. Lett.* **2011**, *2*, 402.

(33) Nakagawa, T.; Beasley, C. A.; Murray, R. W. *J. Phys. Chem. C* **2009**, *113*, 12958.

(34) Guerrini, E.; Piozzini, M.; Castelli, A.; Colombo, A.; Trasatti, S. *J. Solid State Electrochem.* **2008**, *12*, 363.

(35) Trasatti, S.; Lodi, G. In *Electrodes of conductive metallic oxide, Part B*; Trasatti, S., Ed.; Elsevier: Amsterdam, The Netherlands, 1981; p 521.

(36) Krstajić, N.; Trasatti, S. In *Proceedings of the Symposium on Oxygen Electrochemistry*; Adzic, R. R., Anson, F. C., Kinoshita, K., Eds.; The Electrochemical Society: Pennington, NJ, 1996; Vol. *95-26*, p 155.

(37) Grosso, D.; Cagnol, F.; Soler-Illia, G. J. d. A. A.; Crepaldi, E. L.; Amenitsch, H.; Brunet-Bruneau, A.; Bourgeois, A.; Sanchez, C. *Adv. Funct. Mater.* **2004**, *14*, 309.

(38) Wang, Y.; Ren, J.; Wang, Y.; Zhang, F.; Liu, X.; Guo, Y.; Lu, G. *J. Phys. Chem. C* **2008**, *112*, 15293.

(39) Chetty, R.; Scott, K. *Electrochim. Acta* **2007**, *52*, 4073.

(40) Chetty, R.; Scott, K.; Kundu, S.; Muhler, M. *J. Fuel Cell Sci. Technol.* **2010**, *7*, 031011.

(41) Sasaki, K.; Wang, J. X.; Naohara, H.; Marinkovic, N.; More, K.; Inada, H.; Adzic, R. R. *Electrochim. Acta* **2010**, *55*, 2645.

(42) Routray, K.; Zhou, W.; Kiely, C. J.; Wachs, I. E. *ACS Catal.* **2010**, *1*, 54.

(43) Dennis, A. C. *J. Electrochem. Soc.* **1987**, *134*, 377.

(44) Wulf, G. L.; Carter, T. J.; Wallwork, G. R. *Corros. Sci.* **1969**, *9*, 689.

(45) Raghavan, V. *J. Phase Equilib. Diffus.* **2010**, *31*, 369.

(46) Scheffe, J. R.; Li, J.; Weimer, A. W. *Int. J. Hydrogen Energy* **2010**, *35*, 3333.

(47) Perkins, C.; Weimer, A. W. *AIChE J.* **2009**, *55*, 286.

(48) Bañares, M. A.; Wachs, I. E. In *Encyclopedia of Analytical Chemistry*; John Wiley & Sons, Ltd: New York, 2006.

(49) Ivanov, V. G.; Abrashev, M. V.; Iliev, M. N.; Gospodinov, M. M.; Meen, J.; Aroyo, M. I. *Phys. Rev. B* **2010**, *82*, 024104.

(50) Iliev, M. N.; Mazumdar, D.; Ma, J. X.; Gupta, A.; Rigato, F.; Fontcuberta, J. *Phys. Rev. B* **2011**, *83*, 014108.

(51) Ahlawat, A.; Sathe, V. G. *J. Raman Spectrosc.* **2011**, *42*, 1087.

(52) Jehng, J.-M.; Wachs, I. E.; Clark, F. T.; Springman, M. C. *J. Mol. Catal.* **1993**, *81*, 63.

(53) Wu, N.-L.; Kuo, S.-L.; Lee, J.-F.; Sheu, H.-S. *Investigation on Pseudocapacitance Mechanism of MFe_2O_4 Supercapacitors*, National Synchrotron Radiation Research Center - Taiwan Photon Source, 2008.

(54) Chinnasamy, C. N.; Narayanasamy, A.; Ponpandian, N.; Chattopadhyay, K.; Shinoda, K.; Jeyadevan, B.; Tohji, K.; Nakatsuka, K.; Furubayashi, T.; Nakatani, I. *Phys. Rev. B* **2001**, *63*, 184108.

(55) Perron, H.; Mellier, T.; Domain, C.; Roques, J.; Simoni, E.; Drot, R.; Catalette, H. *J. Phys.: Condens. Matter* **2007**, *19*, 346219.

(56) Nordhei, C.; Ramstad, A. L.; Nicholson, D. G. *Phys. Chem. Chem. Phys.* **2008**, *10*, 1053.

(57) Badlani, M.; Wachs, I. E. *Catal. Lett.* **2001**, *75*, 137.